

# The BLOBs: Enigmatic Diffuse Ionized Gas Structures in a Cluster of Galaxies near Cosmic Noon

C. Maier<sup>1</sup>, B. L. Ziegler<sup>1</sup>, and T. Kodama<sup>2</sup>

<sup>1</sup> University of Vienna, Department of Astrophysics, Tuerkenschanzstrasse 17, 1180 Vienna, Austria  
e-mail: christian.maier@univie.ac.at

<sup>2</sup> Astronomical Institute, Tohoku University, Aramaki, Aoba-ku, Sendai 980-8578, Japan

Received ; accepted

## ABSTRACT

We explore the massive cluster XMMXCSJ2215.9-1738 at  $z \sim 1.46$  with MUSE and KMOS integral field spectroscopy. Using MUSE spectroscopy we trace the kinematics of the ionized gas using [O II]  $\lambda\lambda$  3726, 3729 in the central  $500 \times 500 \text{ kpc}^2$  area of the cluster, which contains 28 spectroscopically identified cluster galaxies. We detect [O II]  $\lambda\lambda$  3726, 3729 emission lines in the integrated spectra of 21 galaxies with the remaining seven being passive galaxies. Six of these passive galaxies lie in the cluster central part with a diameter of 200 kpc which contains no star-forming objects, being a place where star-formation in galaxies is quenched. An interesting discovery in this central area of the cluster are three diffuse ionized [O II]  $\lambda\lambda$  3726, 3729 gas structures, which we refer as [OII] blobs, extending over areas of hundreds of  $\text{kpc}^2$ . The source of ionization of one of the gaseous structures which displays two prominent filamentary patterns indicating outflow of gas is an active galactic nucleus (AGN). The KMOS data enabled us to use the BPT diagram to identify this object as a type-2 AGN. The other two diffuse ionized oxygen gaseous structures are more enigmatic, being located between the stellar components of passive cluster galaxies; one of these blobs does not have any stellar counterpart in the HST optical and near-infrared data, and the other only a very faint counterpart. Ram-pressure stripping of photo-ionized gas or AGN feedback could be an explanation. Additionally, the galaxy velocity distribution in this high redshift cluster is bimodal indicating that the cluster is unlikely to be fully virialized, and that recent and ongoing merging events producing shocks could provide photo-ionization sources for the two enigmatic [OII] blobs.

**Key words.** Galaxies: evolution – Galaxies: clusters: general – Galaxies: star formation – Galaxies: clusters: XMMXCSJ2215.9-1738

## 1. Introduction

Environment plays a major role in shaping galaxy evolution. Rich clusters of galaxies in the local and intermediate-redshift Universe are dominated by a quiescent galaxy population composed of ellipticals and lenticulars (e.g., Dressler 1980, 1997). Identifying the dominant physical mechanism responsible for the gas removal and for the subsequent quenching of the star formation activity in cluster galaxies is one of the major questions in galaxy evolution. Different physical processes have been proposed in the literature to explain this, see review by Boselli & Gavazzi (2014). These processes can be broadly divided in two main classes: those related to the gravitational perturbation that a galaxy can suffer in a dense environment (galaxy–galaxy interactions, galaxy–cluster interactions, galaxy harassment) and those due to the hydrodynamical interaction of the interstellar medium (ISM) with the hot and dense intracluster medium (ICM): ram-pressure, thermal evaporation, viscous stripping and starvation. Purely hydrodynamical interactions like ram-pressure leave the stellar body of a galaxy almost undisturbed and only affect its gaseous components, while gravitational interactions act on both.

While local and low-redshift clusters host large fractions of passive galaxies, with increasing redshift the star-forming (SF) population in clusters becomes larger, enabling a study of cluster SF galaxies. Since clusters of galaxies grow by accreting mass from their surroundings, the SF galaxies observed in high- $z$  clusters must be the progenitors of the local passive galaxies. The

$1 < z < 2$  redshift range, which is a transition epoch for clusters, hosts the emergence of the Hubble sequence of disks and elliptical galaxies and the buildup of a significant fraction of the stellar mass in the universe (e.g., Dickinson et al. 2003; Drory et al. 2005). For our studies of environmental effects at  $1 < z < 2$  we selected the  $z \sim 1.46$  cluster XMMXCS J2215.9-1738 (hereafter XMM2215). One advantage for observational environmental studies in this cluster compared to other clusters at  $z > 1$  is its wealth of ancillary data (see Maier et al. 2019, M19 in the following).

Diffuse [O II]  $\lambda\lambda$  3726, 3729 ionized gas traces warm 10 000 K gas. Yuma et al. (2013) introduced a first systematic search for galaxies with spatially extended [O II]  $\lambda\lambda$  3726, 3729 emission (dubbed “[OII] blobs”). They found such blobs to be large up to 75 kpc, and mainly associated with AGN outflows. In a later publication, Yuma et al. (2017) exploited further the number density of [OII] blobs finding this to decrease drastically at  $z < 1.5$  with redshift at a rate that is larger than that of the decrease of cosmic star formation density. At lower redshifts, a serendipitous discovery of a large ionized [OII] gas structure observed in an over-dense region of a galaxy group at redshift  $z \sim 0.7$  was reported by Epinat et al. (2018). In the local Universe, the compact group Stephan’s Quintet was found to contain a 35 kpc intergalactic filamentary structure observed in radio continuum as well as in optical emission lines (ELs) and X-rays (Rodríguez-Baras et al. 2014).

Here we present our investigation of the warm ionized gas in cluster XMM2215 using VLT-MUSE and KMOS

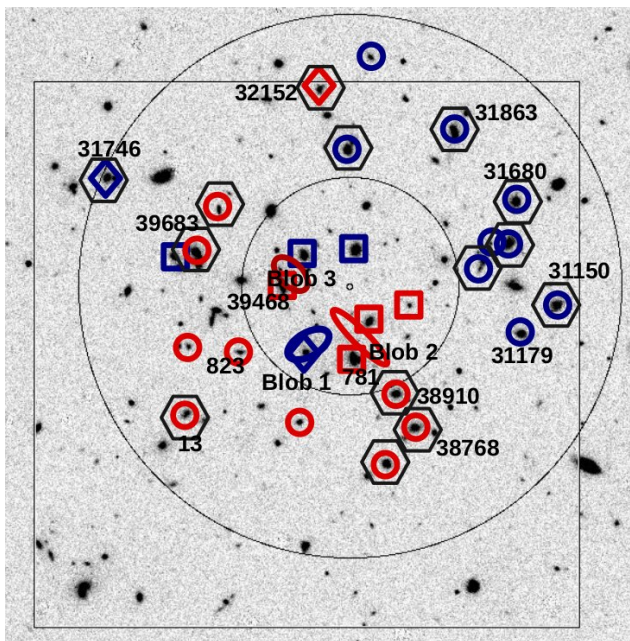


Fig. 1: HST F160W image with the distribution of the 28 cluster members with spectroscopic redshifts in the center of the XMM2215 cluster. The  $500 \times 500 \text{ kpc}^2$  area (at  $z \sim 1.46$ ) covered by MUSE is shown by the large black square. Only the 28 galaxies are shown which lie inside a circular area (indicated by the large black circle) with a radius of 250 kpc around the cluster X-ray center (tiny open black circle). 14 galaxies with  $z < 1.457$  (and 14 at  $z > 1.457$ ) are highlighted in blue (and red); SF galaxies by open circles, three AGN by blue/red rhombus symbols, and passive galaxies by blue/red squares. Written IDs follow the notation used also in M19. The 14 galaxies with ALMA molecular gas measurements are denoted by black hexagons in addition. The rough positions and form of the three blobs of diffuse warm ionized [OII] gas are shown by blue/red ellipses (color depends on the redshift). The smaller black circle with a diameter of  $\sim 200 \text{ kpc}$  around the cluster center is populated only by passive galaxies, an AGN, and the ionized gas blobs, while the galaxies with ALMA molecular gas detections (hexagons) all lie outside this area.

integral field spectroscopic observations. The measurement of [OII]  $\lambda\lambda 3726, 3729$  ELs allows us to study kinematics and to identify [OII] blobs at  $z \sim 1.46$ .

The paper is structured as follows: In Sect. 2 we describe how we performed the data reduction of MUSE and KMOS observations, and how we measured EL fluxes. In Sect. 3 we present our results including the bimodal galaxy velocity distribution in the cluster center, the detection of three “[OII] blobs”, and the properties of the ionized gas of other star-forming galaxies in the central area of the cluster. In Sect. 4 we discuss possible ionization sources for the three [OII] blobs, possible reasons for the quenching of galaxies in the cluster center, and a particular merger event traced by the warm ionized [OII]  $\lambda\lambda 3726, 3729$  gas. We also address caveats and next steps. Finally, we summarize our conclusions. A concordance cosmology with  $H_0 = 70 \text{ km s}^{-1} \text{ Mpc}^{-1}$ ,  $\Omega_0 = 0.25$ ,  $\Omega_\Lambda = 0.75$  is used throughout this paper.

## 2. Observations, data reduction and flux measurements

The cluster XMM2215 is a massive  $z \sim 1.46$  cluster discovered in the XMM Cluster Survey (Stanford et al. 2006), with

extended X-ray emission from the hot gas, suggesting that the cluster is in a relatively advanced evolutionary stage. Estimations of its mass and  $R_{200}$  vary from  $M_{200} = 2.1_{-0.8}^{+1.9} \cdot 10^{14} M_\odot$  and  $R_{200} = (0.8 \pm 0.1) \text{ Mpc}$  (Hilton et al. 2010; Stott et al. 2010) to  $M_{200} = (6.3 \pm 1.2) \cdot 10^{14} M_\odot$  and  $R_{200} = (1.23 \pm 0.18) \text{ Mpc}$  (M19). However, the cluster is unlikely to be fully virialized, as the galaxy velocity distribution is bimodal (see Sect. 3.1), and there is no clear brightest cluster galaxy (Hilton et al. 2009; Stott et al. 2010). The whole wealth of archival ancillary data for this cluster has been recently summarized in detail by Klutse et al. (2024), and we refer to them for details. Here we focus on a description of the XMM2215 data most relevant for our study, which we reduced and analysed ourselves, namely the MUSE and KMOS data.

Observations of the central part of XMM2215 were taken with the MUSE integral field unit using the wide-field adaptive optics (WFM-AO) mode, as part of ESO programme 60.A-9180. In total, the cluster was observed for about 7ks, split into eight 864 s exposures, using the standard spectral range covering  $4770 - 9300 \text{ \AA}$  and a spectral resolution of  $R = \lambda/\Delta\lambda = 4000$  at  $\lambda = 9200 \text{ \AA}$ . We used the raw data from the ESO Science Archive Facility and reduced it using the standard calibrations provided by the ESO-MUSE pipeline, version 1.2.1 (Weilbacher et al. 2020). To reduce the sky residuals, we used an additional tool, the Zurich Atmosphere Purge version 1.0 (ZAP, Soto et al. 2016), on the calibrated cube.

To derive [OII] EL flux and kinematics maps we first extracted for every cluster galaxy and blob a subcube of  $50 \times 50$  spatial spaxels corresponding to  $10 \times 10 \text{ arcsec}^2$ . We used the python code *CAMEL* described in Epinat et al. (2012) to extract ionized gas kinematics of galaxies and blobs by fitting ELs in sub-cubes of  $10 \times 10 \text{ arcsec}^2$  field of view (FoV) around the galaxies or blobs. Before extracting these maps, a spatial smoothing using a 2D Gaussian with a FWHM of three pixels was applied to each data sub-cube in order to increase the signal-to-noise (S/N) ratio. For each spaxel, the [OII] doublet was modelled by two Gaussian profiles sharing the same kinematics (same velocity and same velocity dispersion), but having distinct rest-frame wavelengths ( $3726.04 \text{ \AA}$  and  $3728.80 \text{ \AA}$ ) plus a constant continuum. The variance data cube was used to weight each spectral element during line fitting in order to minimise the effect of noise, which is mainly due to the sky lines. For the three blobs we consider [OII] fluxes and radial velocities for spaxels with [OII] EL fluxes with a  $S/N > 5$ .

In this work we concentrate on the inner part of the cluster almost completely covered by the MUSE data (see Fig. 1). With the assumed cosmology, 1 arcsec corresponds to 8.6 kpc at the mean redshift of the cluster. Thus, the extent of the MUSE FoV is equivalent to  $500 \times 500 \text{ kpc}^2$  at  $z \sim 1.46$ , in the cluster center.

The KMOS H-band observations used to measure the  $H\alpha$  and [NII]  $\lambda 6584$  ELs of  $z \sim 1.46$  cluster galaxies were described in M19. VLT/KMOS YJ-band observations aimed to measure the [OIII]  $\lambda 5007$  and  $H\beta$  ELs were carried out in September 2022 (ESO program ID 109.22VG) with a nod-to-sky strategy and each observing block (OB) consisting of several ABA ABA sequences. The integration time of each exposure was 420 s yielding a total exposure time of 16800 s. The KMOS data reduction for the YJ-data was carried out with the official ESO-KMOS pipeline with the same steps as described in M19 for the KMOS H-band data. To measure the EL flux ratios [NII]  $\lambda 6584/H\alpha$  and [OIII]  $\lambda 5007/H\beta$  needed for the BPT (Baldwin et al. 1981) diagram, we extracted 1D spectra summed over 25 KMOS spaxels centered on the  $H\alpha$  ([OIII]  $\lambda 5007$ ) EL

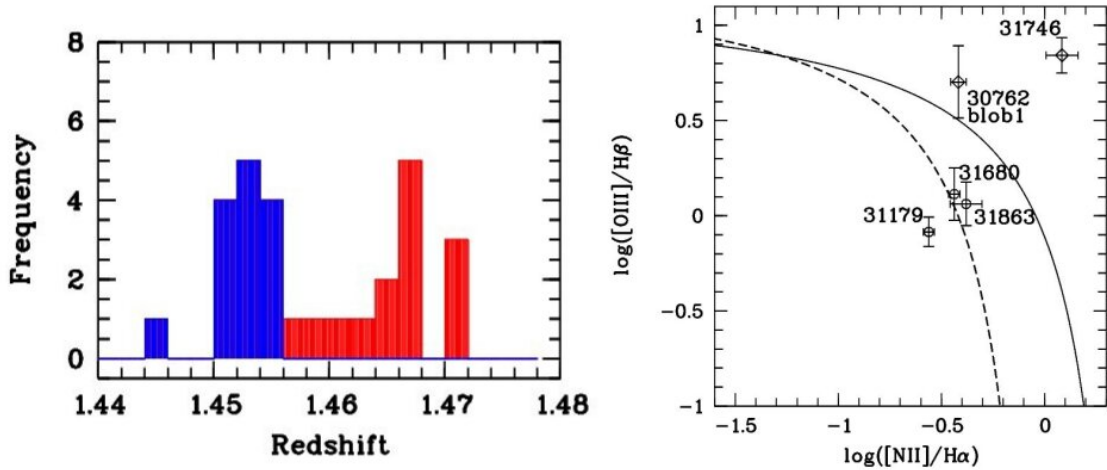


Fig. 2: Left panel: Bimodal distribution for redshifts of 28 cluster galaxies inside a circular area, shown by the large black circle in Fig. 1, with a radius of 250 kpc around the cluster X-ray center. Right panel: Diagnostic diagram BPT (Baldwin et al. 1981) to distinguish star formation-dominated galaxies from AGN for objects with all four ELs observed. The star-forming region of the BPT diagram lies under and to the left of the empirical (dashed) curve of Kauffmann et al. (2003), while the composite region lies between the theoretical (solid) curve of Kewley et al. (2001) and the curve of Kauffmann et al. (2003). Two XMM2215 cluster galaxies are classified as type-2 AGN according to this diagram, two galaxies lie in the composite region and one in the star-forming dominated region. Because KMOS IFUs were only placed on galaxies with stellar counterparts detected on images, which was not the case for blob 2 and blob 3, only blob 1 (object 30762) is depicted in the BPT diagram. Additionally, as further discussed in Sect. 4.5, during KMOS/VLT observations night skylines would have heavily affected some of the ELs needed for the BPT diagram for blob 2 and blob 3, given their redshifts.

of the respective H-band or YJ-band KMOS data cube, see more details in M19. This corresponds to an aperture of 1 square arc-second or  $8.6 \times 8.6 \text{ kpc}^2$  at these redshifts.

### 3. Results

#### 3.1. General properties of XMM2215 cluster galaxies

Fig. 1 depicts the HST F160W image with the distribution of the 28 cluster members with spectroscopic redshifts in the center of the XMM2215 cluster. 14 galaxies with spectroscopic  $z < 1.457$  and 14 at  $z > 1.457$  are highlighted in blue and red. The inner black circle in Fig. 1 comprises the cluster central part around the X-ray cluster center with a diameter of 200 kpc. It contains six passive galaxies with known spectroscopic redshifts (Hilton et al. 2010; Beifiori et al. 2017; Hayashi et al. 2018) and one AGN, galaxy 30762 and corresponding blob 1 (blue rhombus symbol and ellipse). ALMA band 3, 6 and 7 observations (Hayashi et al. 2017; Stach et al. 2017; Hayashi et al. 2018) discovered molecular gas for 14 SF cluster galaxies shown as black hexagons in Fig. 1, and these galaxies with molecular gas detections all lie outside the inner area of the cluster with a diameter of 200 kpc.

A histogram of spectroscopic redshifts shown in the left panel of Fig. 2 indicates a bimodal velocity distribution inside the inner cluster area with a diameter of 500 kpc corresponding to a circular area with a radius of about  $0.25R_{200}$  (large black circle in Fig. 1). Additionally, the 2D distribution of objects in Fig. 1 shows a clear separation in the plane of the sky, corresponding to two kinematically distinct structures, of galaxies with  $z > 1.457$  (red symbols) in the south-east region of the HST image, and  $z < 1.457$  (blue symbols) in the north-west region. With the additional cluster spectroscopic data obtained since 2010 we thus find stronger evidence for this effect, putting

on a firm footing the mild evidence for a bimodal velocity distribution found by Hilton et al. (2010).

#### 3.2. Blob 1: Gas in and around galaxy 30762 hosting an AGN

Blob 1 at  $z \sim 1.453$  at a projected distance of 74 kpc from the X-ray cluster center (see table in M19) has a surface of  $1145 \text{ kpc}^2$ , is located at and around the position of the cluster galaxy 30762, and has EL flux measurements from MUSE and KMOS. The surface area was determined taking into account only spaxels with an [OII] flux with a S/N ratio larger than five.

Fig. 3, left upper panel, shows the position of the stellar component of the 30762 galaxy from HST F160W data compared to the ionized oxygen gas. The MUSE and HST datasets are generally well-aligned in terms of centroid as seen not only for galaxy 30762, but also for other galaxies with more regular [OII] rotation pattern (see figures for objects 31179, 31680, 31150, and 32152 in appendix A). We used the image registration python package and we measured an astrometric offset between the MUSE data and HST of less than 0.2" (the size of a MUSE spaxel). The ionized gas of this blob is extended well beyond the visible stellar component of the galaxy and exhibits two filamentary patterns, one in the north and one in the north-west direction. The north filament has a projected receding velocity of  $\sim 100 \text{ km/s}$  according to the [OII] velocity map, while the north-west filament has a receding velocity of  $\sim 175 \text{ km/s}$ , compared to the blueish area in the center of the blob.

This galaxy was not detected by the ALMA search for molecular gas (Hayashi et al. 2017; Stach et al. 2017; Hayashi et al. 2018), and neither using MeerKAT L-band (1.3 GHz) observations with an integration time of about 12 hours (Klutse et al. 2024). Using Chandra observations of the cluster, Hilton et al. (2010) identified object 30762 as a point X-ray source and inferred an AGN based on its power-law index and its X-ray luminosity. From the derived [NII]/H $\alpha$  EL flux ratio from KMOS (ta-

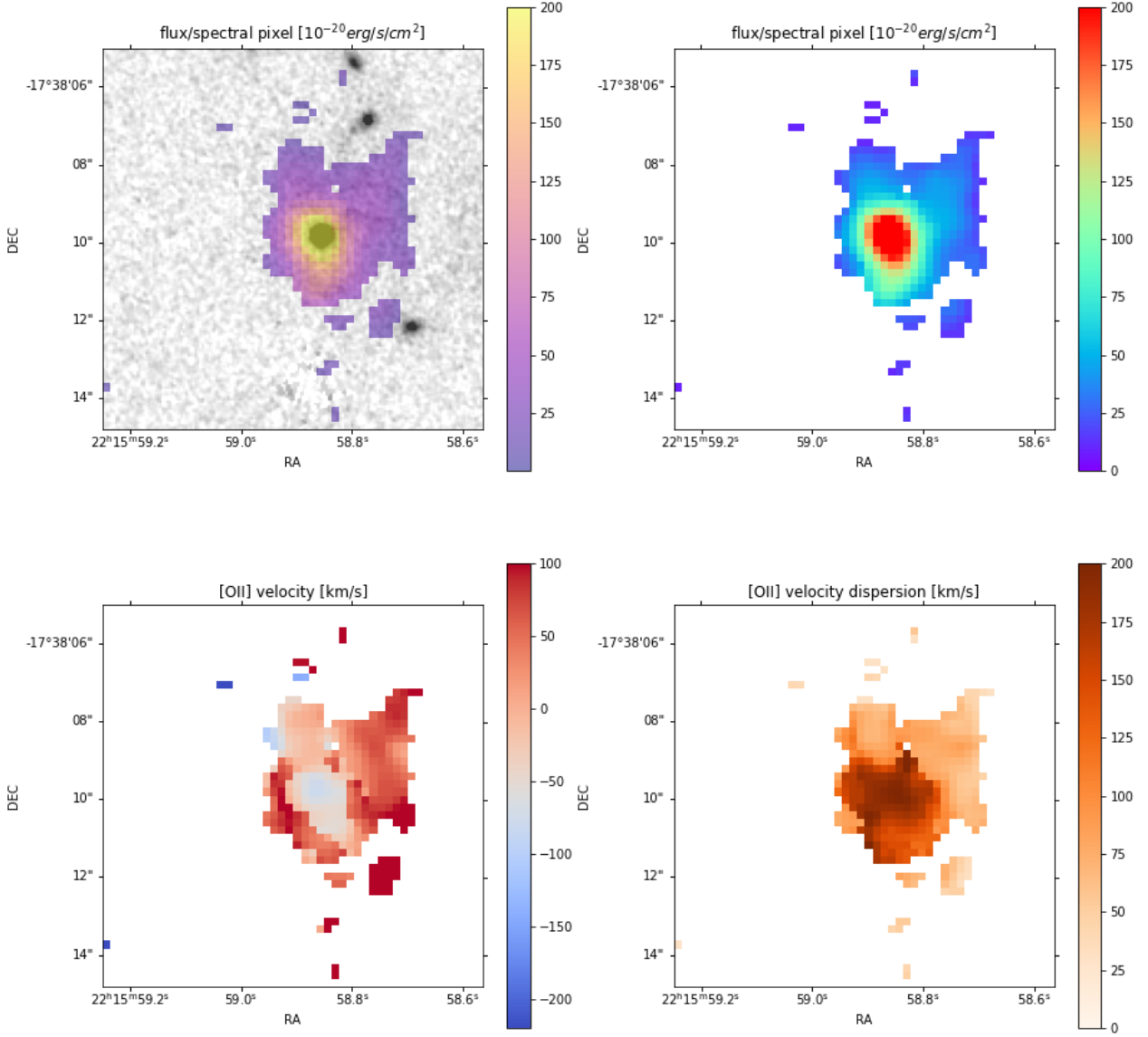


Fig. 3: Clockwise starting at the upper left panel: HST F160W image around the galaxy 30762 (blob 1) with overplotted [OII] EL map; spatially resolved [OII] EL map; spatially resolved [OII] velocity dispersion map; spatially resolved [OII] velocity map. The white background corresponds to spaxels with  $\text{SNR}_{[\text{OII}]} < 5$ .

ble in M19) and our new [OIII]/H $\beta$  EL flux measurement from KMOS YJ-band observations for the central part of the galaxy 30762, we identify this object as a type-2 AGN from the BPT diagram (right panel of Fig. 2).

### 3.3. Blob 2: extended ionized gas with a velocity gradient, but without a stellar component

Blob 2 at  $z \sim 1.466$  has the widest surface ( $1270 \text{ kpc}^2$ ) of the three blobs detected (see Table 1) and is the most puzzling one. It has no stellar counterpart, shows a velocity rotation pattern with a velocity gradient of  $\sim 300 \text{ km/s}$ , and lies between two passive galaxies at similar redshift (see Fig. 4).

Using the relation of Kennicutt (1998) we inferred a SFR of  $1.16 \pm 0.30 \text{ M}_{\odot} \text{ yr}^{-1}$  from the [OII] EL flux of blob 2 assuming that it was related to ionization by young stars. Note that blob 1 discussed in the previous section was proved to contain an AGN,

so we cannot use this method to derive its gas mass, because its EL flux is not only related to ionization by young stars. Using the SFR and the surface of the blob the Kennicutt-Schmidt relation delivers the gas surface density, which allowed us to derive a total gas mass for blob 2 of  $(1.9 \pm 0.5) \times 10^{10} \text{ M}_{\odot}$ . The uncertainties were derived from uncertainties on integrated fluxes and the uncertainty on the slope of the equation from Kennicutt (1998) to transform the [OII] EL flux in SFR. They are dominated by the uncertainty on the slope of the equation from Kennicutt (1998).

The ratio  $[\text{O II}] \lambda 3729 / [\text{O II}] \lambda 3726$  which is resolved by MUSE can be used to derive the gas density of blob 2. This line ratio is  $1.4 \pm 0.1$ , implying a gas density  $n_e \lesssim 10 \text{ cm}^{-3}$  (Osterbrock & Ferland 2006), for the part of the blob which contains the spaxels with the highest [OII] flux (see Fig. 4) and an approaching velocity (blue color). For the rest of the blob with a receding velocity (red color in the velocity plot) the ra-



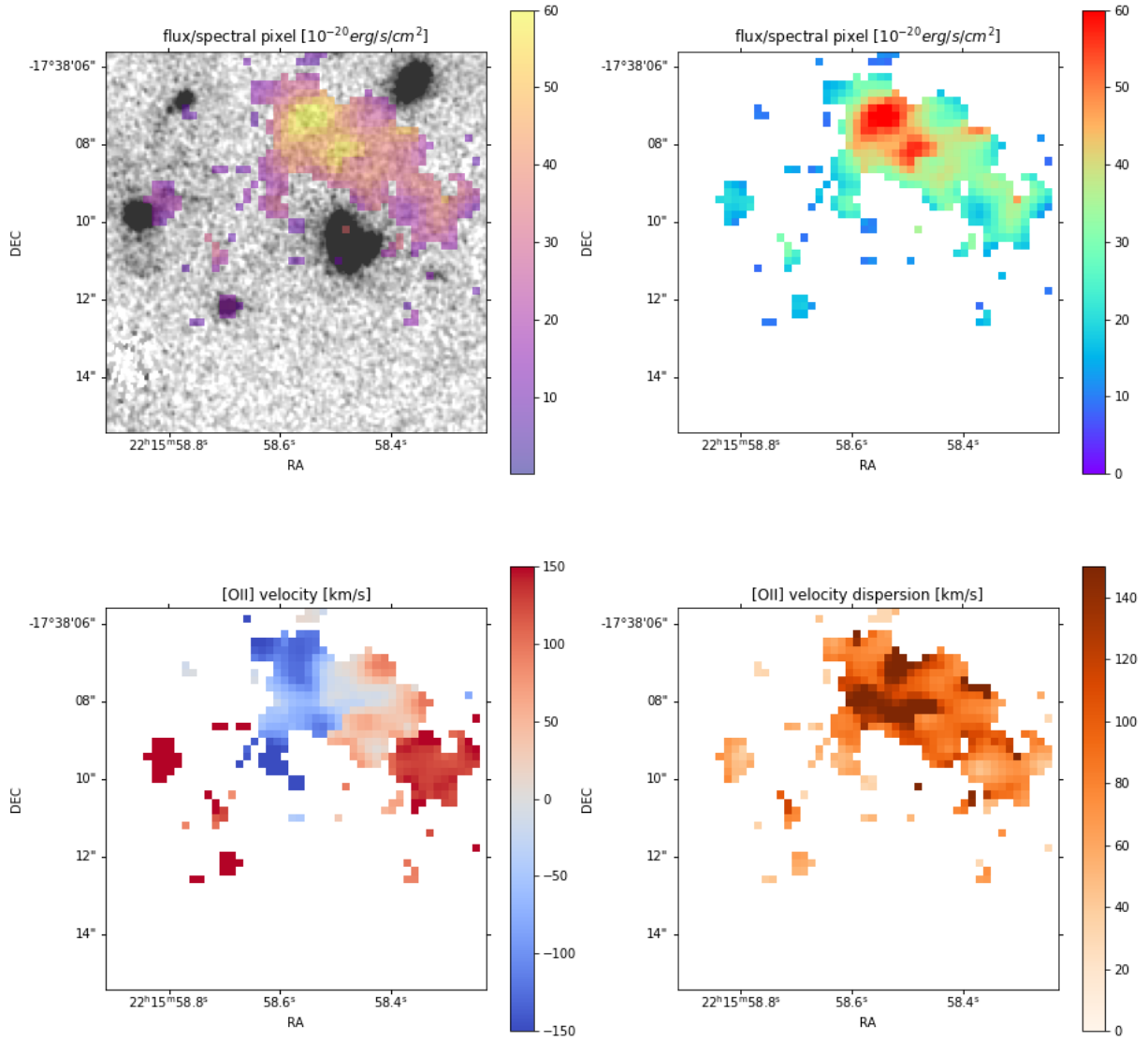


Fig. 4: Clockwise starting at the upper left panel: HST F160W image including blob 2 with overplotted [OII] EL map; spatially resolved [OII] EL map; spatially resolved [OII] velocity dispersion map; spatially resolved [OII] velocity map. The white background corresponds to spaxels with  $\text{SNR}_{[\text{OII}]} < 5$ .

ratio  $[\text{O II}] \lambda 3729/[\text{O II}] \lambda 3726$  is around 1 and lower, implying a higher gas density  $n_e \sim 100\text{--}1000 \text{ cm}^{-3}$ .

### 3.4. Blob 3: ionized gas close to a passive galaxy

Blob 3 at  $z \sim 1.459$  lies close to a passive galaxy at similar redshift (see upper left panel in Fig. 5). It has only a very faint small stellar counterpart, with a diameter of only 0.3 arcsec corresponding to a surface of about  $20 \text{ kpc}^2$ . The blob has a surface of  $571 \text{ kpc}^2$ , being about 30 times larger than the surface of the faint stellar counterpart. It shows a velocity gradient from north to south of about  $120 \text{ km/s}$ , with an extended filamentary tail to the south with an extent of  $\sim 10 \text{ kpc}$ .

Using the procedure described in Sect. 3.3 we inferred for the entire blob a SFR of  $1.08 \pm 0.28 \text{ M}_\odot \text{ yr}^{-1}$  from the [OII] EL flux assuming that it is related to ionization by young stars. The resulting total gas mass is  $(1.4 \pm 0.4) \times 10^{10} \text{ M}_\odot$ .

### 3.5. Other galaxies

We detected [OII] in the integrated spectra for all 18 SF cluster galaxies with known spectroscopic redshifts in the MUSE area (see Fig. 1) and for the 3 AGN. Given the MUSE integration time of less than two hours, the S/N per spaxel of the [OII] emission is often quite low, preventing kinematics studies of about half of the SF XMM2215 cluster galaxies. We present the kinematic diagrams in the appendix A for nine SF galaxies and two type-2 AGN (object 32152 identified as type-2 AGN by M19, and object 31746 identified as type-2 AGN from BPT diagram Fig. 2). These objects show a regular rotation pattern and a quite regular ionized gas distribution coinciding with the galaxy stellar component, with the exception of objects 38768 and 39683 (Figs. A.3 and A.5), although when considering less reliable detections at lower S/N for these two objects.

On the other hand, there is one galaxy 31863 at a projected distance of  $185 \text{ kpc}$  in the north-west direction from the X-ray

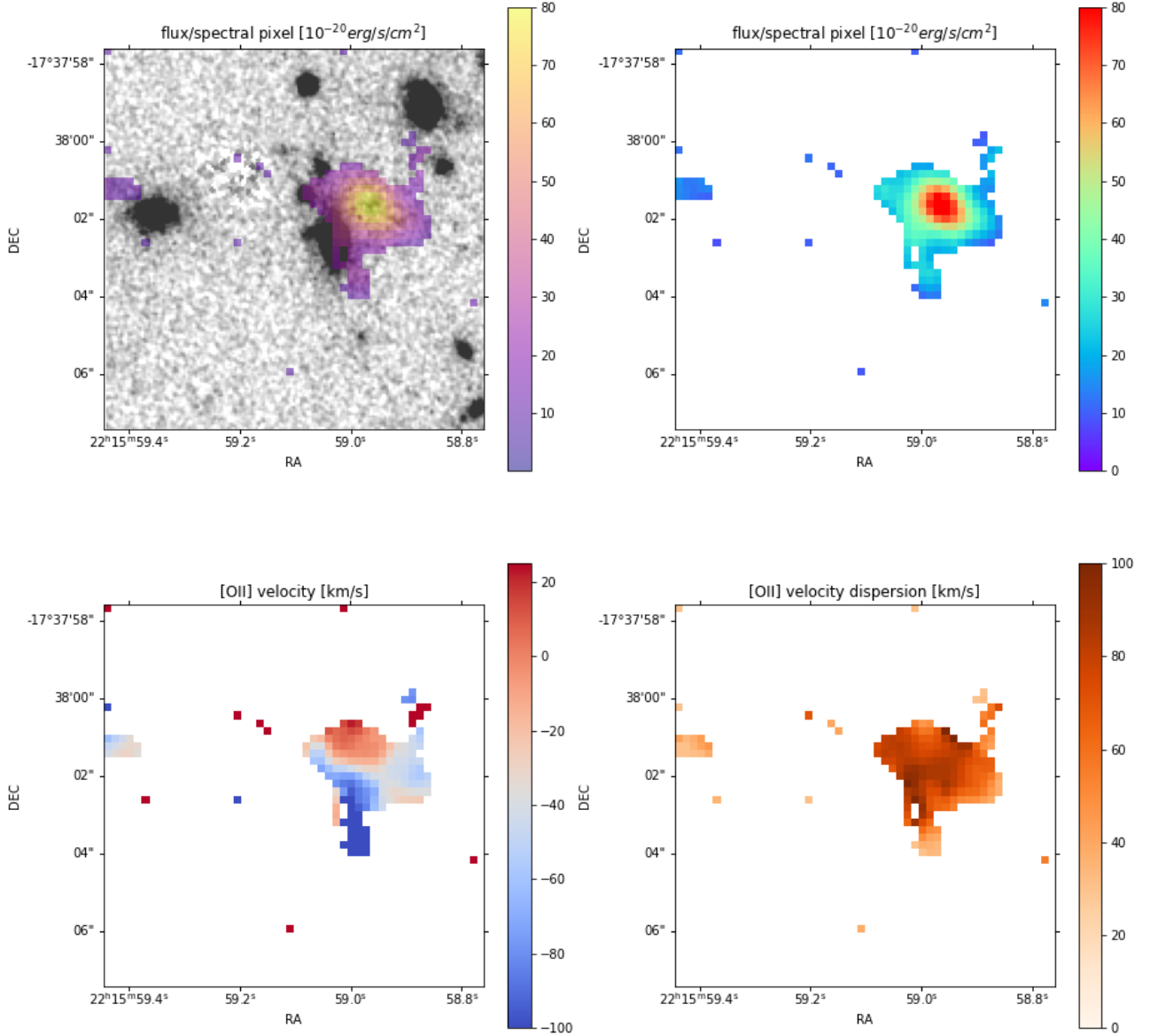


Fig. 5: Clockwise starting at the upper left panel: HST F160W image including blob 3 with overplotted [OII] EL map; spatially resolved [OII] EL map; spatially resolved [OII] velocity dispersion map; spatially resolved [OII] velocity map. The white background corresponds to spaxels with  $\text{SNR}_{[\text{OII}]} < 5$ .

cluster center with a more particular kinematic map (see Fig. 6). Object 31863 is a SF galaxy at  $z \sim 1.452$  with measurements of several ELs with KMOS and MUSE. In the BPT diagram it lies in the AGN/SF composite region (see Fig. 2). Its molecular gas mass derived from ALMA observations is  $3.5 \pm 0.5 \times 10^{10} M_{\odot}$  (Hayashi et al. 2018). Fig. 6 shows an elongated [OII] emission region extended on both sides of the galaxy in a filamentary structure of about 60 kpc projected length on each side. Apart from the central stellar counterpart representing galaxy 31863, there is a smaller stellar counterpart in the northern part of the elongated [OII] gas emission, while no stellar counterpart is seen in the HST image for the southern part of the ionized gas.

The ratio  $[\text{O II}] \lambda 3729 / [\text{O II}] \lambda 3726$  can be used to derive the gas density of the galaxy 31863. The typical line ratio measured for the gas around the central stellar counterpart (galaxy 31863) is about 1.5, implying a gas density  $n_e \sim 10 \text{ cm}^{-3}$  (Os-

terbrock & Ferland 2006). A similar  $[\text{O II}] \lambda 3729 / [\text{O II}] \lambda 3726$  ratio is measured for the southern part of the gas, which has a receding velocity of the gas of about 200 km/s (red color in the velocity map), and does not have a stellar counterpart. For the northern part of the gas with an approaching velocity of about 200 km/s (blue color) the ratio  $[\text{O II}] \lambda 3729 / [\text{O II}] \lambda 3726$  is smaller,  $0.8 \pm 0.2$ . This implies a higher gas density  $n_e \sim 400\text{--}1000 \text{ cm}^{-3}$ , for the northern part of the gas which also has a stellar counterpart, albeit smaller than galaxy 31863. The typical recombination time of the ionized gas can be calculated as  $\tau_{\text{rec}} = 1/n_e \alpha_A$  where  $\alpha_A$  is the total recombination coefficient  $\alpha_A = 4.2 \times 10^{-13} \text{ cm}^3 \text{ s}^{-1}$  (Osterbrock & Ferland 2006). For  $n_e = 10 \text{ cm}^{-3}$ , this results in  $\tau_{\text{rec}} \approx 10^4 \text{ yrs}$ , while for  $n_e = 400\text{--}1000 \text{ cm}^{-3}$ , this implies  $\tau_{\text{rec}} \approx 100\text{--}250 \text{ yrs}$ .

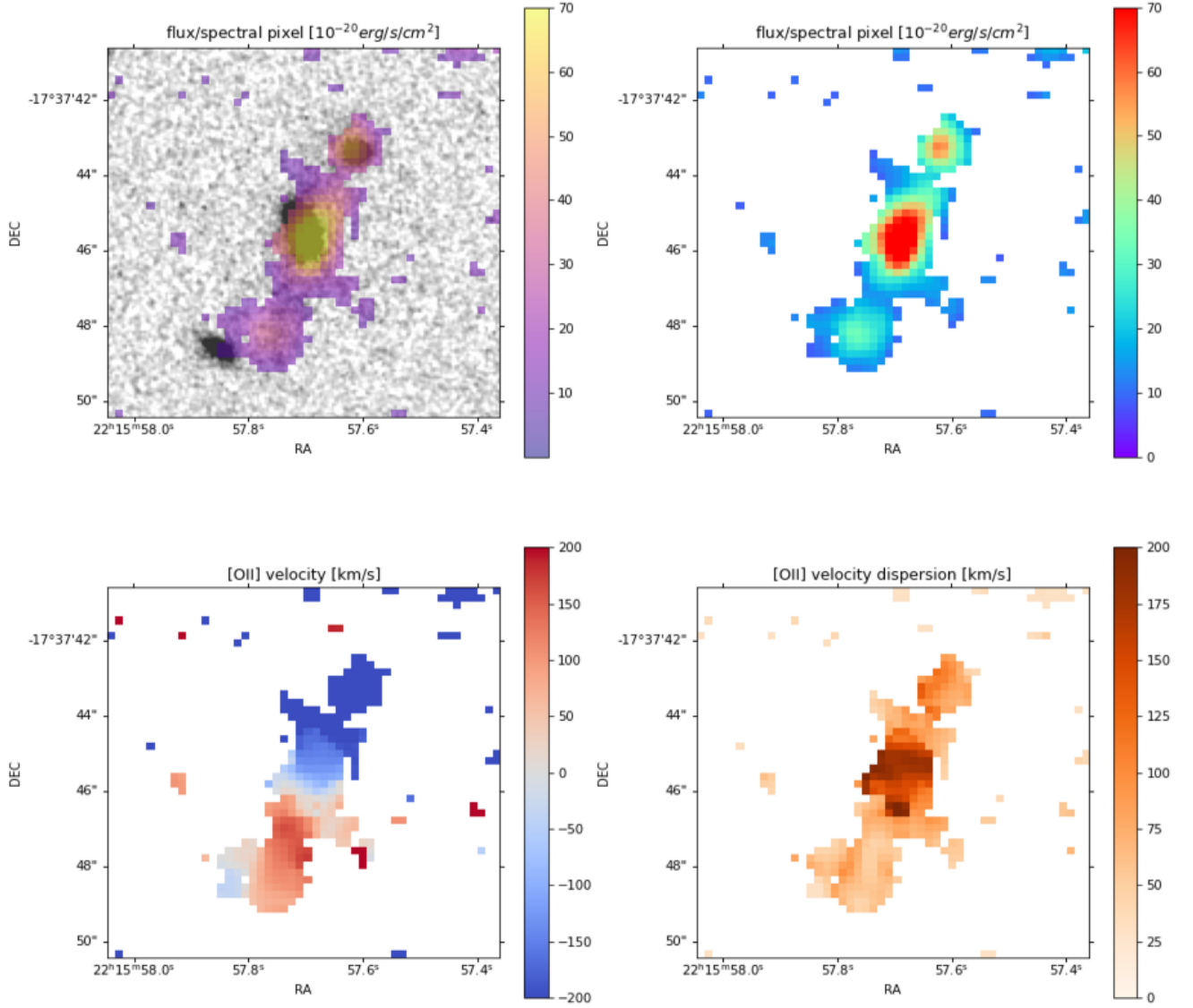


Fig. 6: Clockwise starting at the upper left panel: HST F160W image around the galaxy 31863 with overplotted [OII] EL map; spatially resolved [OII] EL map; spatially resolved [OII] velocity dispersion map; spatially resolved [OII] velocity map. The white background corresponds to spaxels with  $\text{SNR}_{[\text{OII}]} < 4$ .

Table 1: Properties of the three detected [OII] blobs. The integrated [OII] flux is given in units of  $10^{-17} \text{ erg s}^{-1} \text{ cm}^{-2}$ .

Id	RA	DEC	Redshift	Surface	[OII]	Peculiarities
Blob1	22:15:58.843	-17:38:09.98	1.453	1145 $\text{kpc}^2$	$23.3 \pm 3.6$	X-ray AGN
Blob2	22:15:58.440	-17:38:08.64	1.466	1270 $\text{kpc}^2$	$7.1 \pm 1.8$	no stellar component
Blob3	22:15:58.972	-17:38:02.04	1.459	571 $\text{kpc}^2$	$5.9 \pm 1.5$	close to a passive galaxy

## 4. Interpretation

### 4.1. Blob 1: Active AGN 30762 becoming BCG of the cluster?

The ionized gas of blob 1 shows two filamentary patterns, one in the north and one in the north-west direction. These filamentary patterns of the ionized gas are indicative for outflow of gas with a projected velocity of  $\sim 100 \text{ km/s}$  and  $\sim 175 \text{ km/s}$ , respectively. Since there is no ALMA molecular gas detection for this galaxy, and given the high about solar gas metallicity (cf. Bergemann et al. 2021) derived by M19 (albeit in the central region) for object 30762, we think that inflow of gas in the two filamen-

tary regions is unlikely and that the two filamentary structures trace outflow of gas.

On its journey through the cluster, this galaxy 30762 hosting an AGN may have interacted with other SF galaxies and may have expelled gas from them, producing [OII] blobs. Here is a possible scenario, whose correctness could be verified by new future simulations of forming clusters around cosmic noon, following galaxies travelling through the cluster, including warm gas like the [OII] ionized gas we detected.

In the past, moving through the cluster, AGN 30762 may have interacted with galaxy 781 near blob 2 and may have ex-

pelled gas from galaxy 781, which is passive today (Beifiori et al. 2017). Due to proper motions of galaxies in the cluster, this possibly happened at an apparent redshift of  $z \sim 1.460$ . Note that blob 1 (blue ellipse) and blob 2 (larger red ellipse) are close to each other and even partly slightly overlapping in projection (see Fig. 1). Continuing its journey into our line-of-sight direction, AGN 30762 appears due to its proper motion at redshift  $z \sim 1.453$  now, while the outflowing receding gas flow in the opposite direction through the cluster reaching a redshift  $z \sim 1.466$ . We see the projection of the gas outflowing as blob 2 with a proper motion of the gas inducing a projected line-of-sight velocity difference of around  $300 \text{ km s}^{-1}$  ([OII] velocity map in Fig. 4). The gas in blob 2 could be due either to a reservoir fed by outflows from the AGN 30762, or to gas stripped from galaxy 781 during the interaction with AGN 30762 and gas stripped from galaxy 781 due to RPS in the inner region of the cluster, and then trapped by the gravitational potential of blob 2. This would be in line with an AGN-RPS synergy quenching scenario advocated by Maier et al. (2022) for the inner regions of clusters at intermediate redshifts.

This galaxy 30762 hosting an AGN lies at a projected distance of 74 kpc from the X-ray cluster center and is a good candidate to become the (active) brightest cluster galaxy (BCG) of the cluster XMM2215, by reaching the X-ray center of the cluster in the future (cf., e.g., simulations by Muldrew et al. 2018). With a velocity of  $\sim 1000 \text{ km/s}$  (as derived by M19) corresponding to about  $1 \text{ kpc/Myr}$  it could reach the X-ray center in about 0.1 Gyr.

#### 4.2. Blob 2: Outflowing gas or stripped gas or shocks?

Blob 2 at  $z \sim 1.466$  has no stellar counterpart, shows a velocity rotation pattern, and lies between two passive galaxies at similar redshift (see Fig. 4). The typical line ratio measured pixel per pixel for the east part with an approaching velocity (blue color in the velocity map) is about 1.5, implying a gas density  $n_e \lesssim 10 \text{ cm}^{-3}$  (Osterbrock & Ferland 2006). This is the part of the blob with the highest [OII] emission and the highest velocity dispersion, as shown in Fig. 4. The total recombination coefficient for this density is  $\tau_{\text{rec}} \approx 10^4 \text{ yrs}$ . This quite short recombination time implies that a source of gas excitation must be present in the gas component. Shocks could be an explanation, as also suggested by the high velocity dispersion in this region.

The large ionized gas mass of blob 2 of  $(1.9 \pm 0.5) \times 10^{10} M_{\odot}$  derived in Sect. 3.3 and the absence of stars indicate that gas might be stripped from galaxy 781 during interactions or merger events, and trapped by the gravitational potential of the structure, like in the scenario discussed in Sect. 4.1. This quite large gas mass is typical for SF galaxies with stellar masses of a few  $10^{10} M_{\odot}$  (e.g., Cybulsky et al. 2017), like the passive galaxy 781 in the vicinity of blob 2 and at a similar redshift. Blob 2 lies at a projected distance of about 70 kpc from the X-ray cluster center. The cluster central part with a diameter of 200 kpc (inner black circle in Fig. 1) contains six passive galaxies with known spectroscopic redshifts (Hilton et al. 2010; Beifiori et al. 2017; Hayashi et al. 2018) and the three blobs. This inner area of the cluster with a radius of 100 kpc is a region where SF galaxies stop their star formation probably due to different processes. Likely candidates are mergers, ram-pressure stripping (RPS) and shocks.

We are not aware of any simulations papers on cool gas ( $T \sim 10000 \text{ K}$ ) in galaxy clusters near cosmic noon by now. Very recently, a first step in this direction was done by a simulations paper on cool gas in galaxy clusters at redshift zero (Staffehl et

al. 2025). They combined the TNG-Cluster and TNG300 cosmological magnetohydrodynamical simulations to study cool gas in local galaxy clusters. If these theoretical studies of cool gas in clusters will be extended to higher redshifts (near cosmic noon), our slightly speculative scenarios for the [OII] blobs discovered in XMM2215 could be verified.

#### 4.3. Blob 3: ionized gas stripped by RPS or shocks?

Blob 3 at  $z = 1.459$  is located near the passive galaxy 39468, at a projected distance of 62 kpc from the X-ray cluster center. This ionized gas might be the result of RPS acting on the galaxy 39468 in the past when the galaxy entered the inner region of the cluster. As mentioned before, the cluster central part with a diameter of 200 kpc contains six passive galaxies (including 39468), being a region of the cluster where star formation in galaxies is quenched. The very faint stellar counterpart in the center of blob 3 could be star formation induced in the stripped gas, as observed during RPS of gas at lower redshifts.

Assuming that it is related to ionization by young stars, a total gas mass of  $(1.4 \pm 0.4) \times 10^{10} M_{\odot}$  was inferred for this blob. However, given the faintness of the stellar counterpart, it is quite unlikely that this is the only source for ionization of blob 3. Therefore, additional ionization due to shocks from past and ongoing merger events could be an explanation.

While the photo-ionization of blob 1 is related to the AGN in the galaxy 30762, the photo-ionization of blob 2 and blob 3 could have diverse origins and it remains enigmatic. Galaxy interactions may induce shocks through the gas flows that are caused by the merger process (Rich et al. 2015). Photo-ionization can be powered by an AGN as well, which can be fuelled with gas driven inwards by tidal forces during mergers. The galaxy velocity distribution in cluster XMM2215 is bimodal (Figs. 1 and 2), so mergers and shocks are very probable. Nevertheless, the enigmatic origin of the photo-ionization of blob 2 and blob 3 has to be addressed also with new future improved simulations of forming clusters around cosmic noon, including not only the hot gas component, but also warm gas like the [OII] ionized gas we detected.

#### 4.4. Object 31863: merger event

Galaxy 31863 is a SF galaxy at  $z \sim 1.452$  at a projected distance of 185 kpc from the X-ray cluster center. It has an elongated [OII] emission region extended on both sides of the galaxy (see Fig. 6) in a filamentary structure of about 60 kpc projected length on each side. The density analysis in Sect. 3.5 implies a higher gas density  $n_e \sim 400\text{--}1000 \text{ cm}^{-3}$  for the northern part of the gas compared to the central and southern part. The typical recombination time of the ionized gas for this density is  $\tau_{\text{rec}} \approx 100 - 250 \text{ yrs}$ .

The very short recombination time  $\approx 100 - 250 \text{ yrs}$  for the northern part of the gas implies that a source of gas excitation must be present in the gas. A smaller stellar counterpart for the northern part is visible on the HST image, and we call this smaller galaxy 31863b. The southern part of the gas has a higher recombination time  $\tau_{\text{rec}} \approx 10^4 \text{ yrs}$ , and no stellar counterpart. It represents most likely an outflow of gas produced by a central starburst fed by the collapse of gas induced by the merging process of galaxies 31863 and 31863b. The brightest [OII] regions seen in the central part of the gas support this central starburst scenario.



#### 4.5. Caveats and next steps

The BPT line diagnostic diagram is useful to constrain sources for photo-ionization, e.g., the presence of shocks. However, only five galaxies from our studied sample have all EL measurements needed to be depicted in the BPT diagram (see Fig. 2, right panel). The reason for the very small percentage of objects (5 out of the 19 galaxies studied by M19) with measurements plotted in the BPT diagram is that, at  $z \sim 1.5$ , at least one of the four ELs [NII] $\lambda$ 6584, H $\alpha$ , [OIII] $\lambda$ 5007, or H $\beta$ , needed to explore ionizing conditions in the BPT diagram, is heavily affected by strong night sky lines (see also table in M19) when using near-infrared spectroscopy at  $1 - 2\mu\text{m}$  from ground-based telescopes like VLT. This shows the absolute need for James Webb Space Telescope (JWST) observations which is the only current telescope able to provide the measurements of all four EL fluxes free of strong night sky lines for a statistically significant number of cluster galaxies at these redshifts.

The integration time for the MUSE data was less than two hours. Although enigmatic and interesting blobs with brighter [OII] ELs could be identified and also used for kinematics, for about half of the SF cluster galaxies observed with MUSE no kinematic studies were possible because of fainter ELs and low S/N of the [OII] flux in single spaxels. Therefore, deeper MUSE observations would be an asset to study kinematics of all known spectroscopic SF cluster members in the inner part of XMM2215.

### 5. Summary and Conclusions

Using VLT-MUSE integral field spectroscopy, we investigated the central  $500 \times 500 \text{ kpc}^2$  area of the XMM2215 cluster at  $z \sim 1.46$ , which contains 28 spectroscopically identified cluster galaxies. Our analysis was complemented with VLT-KMOS observations for some objects, and other archival ancillary data. Our principal findings can be summarized as follows:

1. We detected [O II]  $\lambda\lambda$  3726, 3729 emission lines in the integrated spectra of 21 galaxies, while the remaining seven are passive galaxies. The cluster central part with a diameter of 200 kpc (inner black circle in Fig. 1) contains six passive galaxies being a region where star-formation in galaxies is quenched.
2. The galaxy velocity distribution in this high redshift cluster is bimodal (see Figs. 1 and 2) indicating that the cluster is unlikely to be fully virialized, and that ongoing merging events possibly develop shocks which could be a source of photo-ionization.
3. We discovered three diffuse ionized [O II]  $\lambda\lambda$  3726, 3729 gas structures which we call [OII] blobs, in the central area of the cluster with a radius of 100 kpc.
4. Blob 1 with its stellar counterpart galaxy 30762 at  $z \sim 1.453$  has a surface of  $1145 \text{ kpc}^2$  and lies at a projected distance of 74 kpc from the X-ray cluster center. The source of ionization of the blob is an AGN, with the galaxy being X-ray detected and classified as a type-2 AGN from the BPT diagram. The blob displays two prominent filamentary patterns indicating outflow of gas with a projected velocity of  $\sim 100 \text{ km/s}$  and  $\sim 175 \text{ km/s}$ , respectively (see Fig. 3). This galaxy is a good candidate to become the BCG of the cluster in the near future.
5. Blob 2 at  $z \sim 1.466$  with a surface of  $1270 \text{ kpc}^2$  is the most puzzling of the three blobs. It has no stellar counterpart, shows a velocity rotation pattern with a velocity gradient of

$\sim 300 \text{ km/s}$ , and lies between two passive galaxies at similar redshift (see Fig. 4). We discussed a possible formation and photo-ionization scenario related to AGN 30762 travelling through the cluster and interacting with galaxy 781 close to blob 2. Additionally, shocks from past and ongoing merger events indicated by the bimodal velocity distribution in this cluster could be a source of photo-ionization.

6. Blob 3 at  $z \sim 1.459$  has a surface of  $571 \text{ kpc}^2$  and is located near the passive galaxy 39468 (see Fig. 5) at a projected distance of 62 kpc from the X-ray cluster center. We interpret the blob to be the result of a mix of RPS acting on the galaxy 39468 in the past when the galaxy entered the inner region of the cluster, and shocks from past and ongoing merger events indicated by the bimodal velocity distribution in this cluster.
7. We also analysed a galaxy 31863 at a projected distance of 185 kpc in the north-west direction from the X-ray cluster center with a more particular kinematic map. The density and recombination time analysis for this object revealed that a stellar counterpart of the northern part of the gas must be a source of gas excitation representing a smaller galaxy 31863b in an merging process with 31863. We interpret the southern part of the gas as outflow of gas produced by a central starburst fed by the collapse of gas induced by the merging process.

To extend this analysis to more cluster galaxies, and to further explore photo-ionization sources of the enigmatic blobs 2 and 3, JWST observations to overcome night-sky line contamination of EL fluxes required for the BPT diagram and deeper MUSE observations are needed. Note that we used MUSE observations with an integration time of only less than two hours for this work. To further explore the origin of the enigmatic blobs, better simulations of forming clusters around cosmic noon are also needed, including not only the hot gas component, but also warm gas, to be compared with the warm ionized gas blobs we are observing in XMM2215.

*Acknowledgements.* We would like to thank the anonymous referee for providing constructive comments and help in improving the manuscript. TK acknowledges financial support from JSPS KAKENHI Grant Number 24H00002 (Specially Promoted Research by T. Kodama et al.)

### References

- Bacon, R., Piqueras, L., Conseil, S., et al. 2016, *Astrophysics Source Code Library* [record ascl:1611.003]
- Baldwin, J. A., Phillips, M. M., & Terlevich, R., 1981, *PASP*, 93, 5
- Beifiori, A., Mendel, J. T., Chan, J. C. C., et al. 2017, *ApJ*, 846, 120
- Bergemann, M., Hoppe, R., Semenova, E., et al., 2021, *MNRAS*, 508, 2236
- Boselli, A. & Gavazzi, G., 2014, *A&ARv*, 22, 74
- Cybulski, R., Yun, M. S., Erickson, N., et al. 2016, *MNRAS*, 459, 3287
- Dickinson, M., Papovich, C., Ferguson, H. C., et al., 2003, *ApJ*, 587, 25
- Drory, N., Salvato, M., Gabasch, A., et al., 2005, *ApJ*, 619, 131
- Dressler, A. 1980, *ApJ*, 236, 351
- Dressler, A., Oemler, Jr., A., Couch, W. J., et al. 1997, *ApJ*, 490, 577
- Epinat, B., Tasca, L., Amram, P. et al. 2012, *A&A*, 539, A92
- Epinat, B., Contini, T., Finley, H. et al. 2018, *A&A*, 609, A40
- Hayashi, M., Kodama, T., Kohno, K., et al., 2017, *ApJ*, 841, L21
- Hayashi, M., Tadaki, K.-i., Kodama, T., et al., 2018, *ApJ*, 856, 118
- Hilton, M., Stanford, S. A., Stott, J. P., et al. 2009, *ApJ*, 697, 436
- Hilton, M., Lloyd-Davies, E., Stanford, S. A., et al. 2010, *ApJ*, 718, 133
- Kauffmann, G., Heckman, T. M., White, S. D. M., et al., 2003, *MNRAS*, 341, 33
- Kenicutt, R. C., Jr. 1998, *ARA&A*, 36, 189
- Kewley, L. J., et al., 2001, *ApJS*, 132, 37
- klutse, D. Y., Hilton, M., Heywood, I., et al., 2024, *MNRAS*, 532, 2842
- Maier, C., Hayashi, M., Ziegler, B. L., & Kodama, T., 2019, *A&A*, 626, A14
- Maier, C., Haines, C. P., & Ziegler, B. L., 2022, *A&A*, 658, A190
- Muldrew, S. I., Hatch, N. A., & Cooke, E. A., 2018, *MNRAS*, 473, 2335

- Osterbrock, D. E., & Ferland, G. J. 2006, in *Astrophysics of Gaseous Nebulae and Active Galactic Nuclei*, 2nd edition, eds. D. E. Osterbrock, & G. J. Ferland (Sausalito, CA: University Science Books)
- Rich, J. A., Kewley, L. J., Dopita, M. A., 2015, *ApJS*, 221, 28
- Rodríguez-Baras, M., Rosales-Ortega, F. F., Díaz, A. I., 2014, *MNRAS*, 442, 495
- Soto K. T., Lilly S. J., et al., 2016, *MNRAS*, 458, 3210
- Stach, S. M., Swinbank, A. M., Hilton, M. et al. 2017, *ApJ*, 849, 154
- Staffehl, M., Nelson, D., Ayromlou, et al., 2025, *arXiv:2503.01960*
- Stanford, S. A., Romer, A. K., Sabirli, K., et al. 2006, *ApJL*, 646, L13
- Stott, J. P., Collins, C. A., Sahlén, M., et al. 2010, *ApJ*, 718, 23
- Weilbacher P. M., Palsa, R., Streicher O., et al., 2020, *arXiv:2006.08638*
- Yuma, S., Ouchi, M., Drake, A. B., et al. 2013, *ApJ*, 779, 53
- Yuma, S., Ouchi, M., Drake, A. B., et al. 2017, *ApJ*, 841, 93

## Appendix A: EL flux and velocity maps

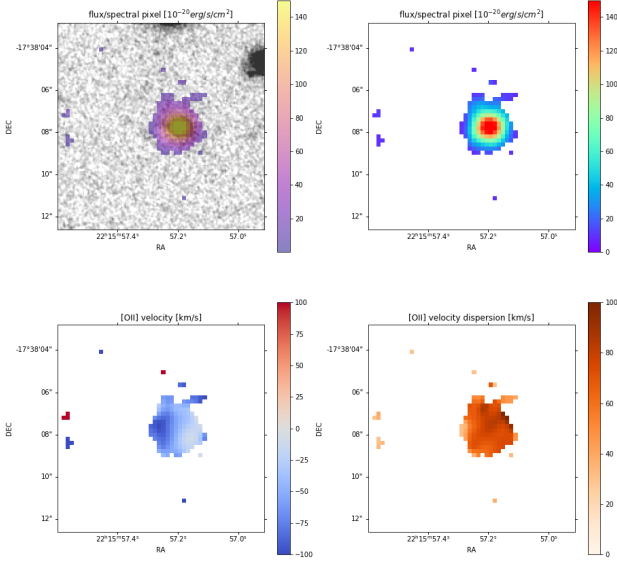


Fig. A.1: Clockwise starting at the upper left panel: HST F160W image around the galaxy 31179 with overplotted [OII] EL map; spatially resolved [OII] EL map; spatially resolved [OII] velocity dispersion map; spatially resolved [OII] velocity map. The white background corresponds to spaxels with  $\text{SNR}_{[\text{OII}]} < 5$ .

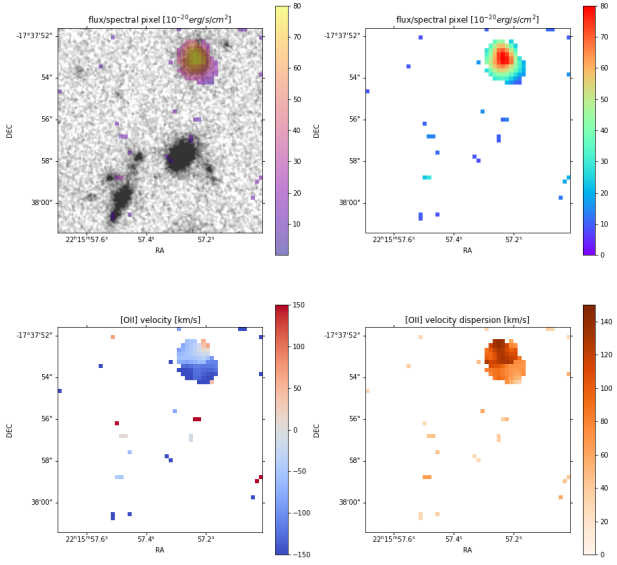


Fig. A.2: Clockwise starting at the upper left panel: HST F160W image including the galaxy 31680 in the north-west corner of the image and three other galaxies with fainter [OII], with overplotted [OII] EL map; spatially resolved [OII] EL map; spatially resolved [OII] velocity dispersion map; spatially resolved [OII] velocity map. The white background corresponds to spaxels with  $\text{SNR}_{[\text{OII}]} < 5$ . From ALMA, galaxy 31680 has a derived molecular gas mass of  $8.1^{+0.6}_{-0.5} \times 10^{10} M_{\odot}$  (Hayashi et al. 2018). Two other galaxies in the figure have lower ALMA molecular gas mass measurements of  $(2.7 \pm 0.6) \times 10^{10} M_{\odot}$  and  $(5.8 \pm 0.6) \times 10^{10} M_{\odot}$ , but they are not detected in [OII] in the individual spaxels above the S/N cut limit.

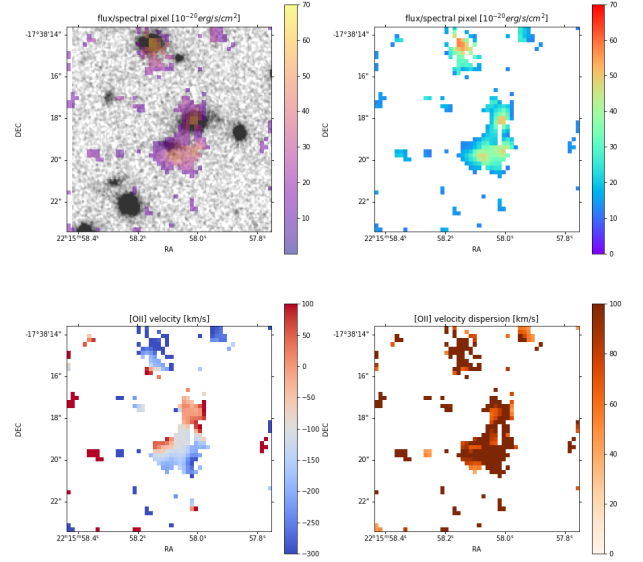


Fig. A.3: Clockwise starting at the upper left panel: HST F160W image including the galaxy 38910 in the north-west upper part of the image and 38768 in the center, with overplotted [OII] EL map; spatially resolved [OII] EL map; spatially resolved [OII] velocity dispersion map; spatially resolved [OII] velocity map. The white background corresponds to spaxels with  $\text{SNR}_{[\text{OII}]} < 3$ . From ALMA, galaxy 38768 has a derived molecular gas mass of  $(3.1 \pm 0.6) \times 10^{10} M_{\odot}$  (Hayashi et al. 2018).

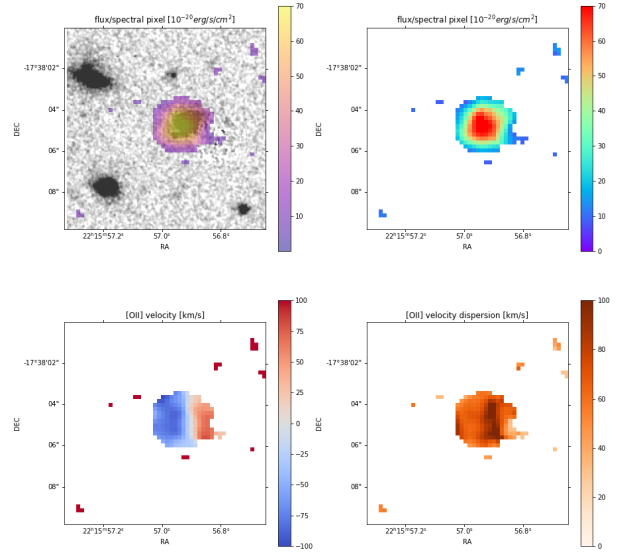


Fig. A.4: Clockwise starting at the upper left panel: HST F160W image around the galaxy 31150 with overplotted [OII] EL map; spatially resolved [OII] EL map; spatially resolved [OII] velocity dispersion map; spatially resolved [OII] velocity map. The white background corresponds to spaxels with  $\text{SNR}_{[\text{OII}]} < 5$ .

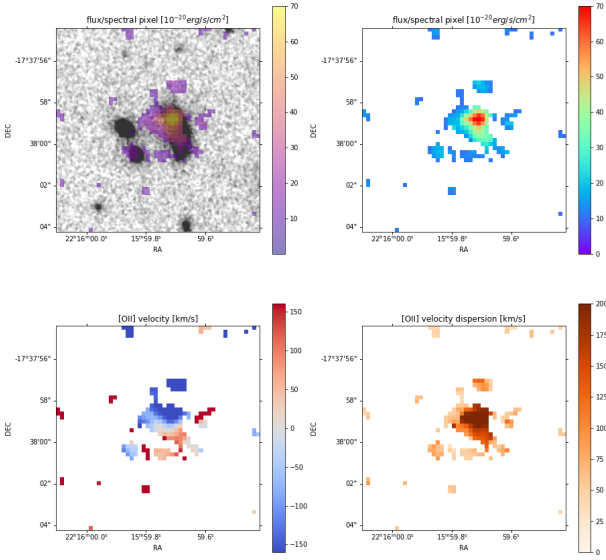


Fig. A.5: Clockwise starting at the upper left panel: HST F160W image around the galaxy 39683 with overplotted [OII] EL map; spatially resolved [OII] EL map; spatially resolved [OII] velocity dispersion map; spatially resolved [OII] velocity map. The white background corresponds to spaxels with  $\text{SNR}_{[\text{OII}]} < 3$ . From ALMA, galaxy 39683 has a derived molecular gas mass of  $10.5^{+0.7}_{-0.5} \times 10^{10} M_{\odot}$  (Hayashi et al. 2018).

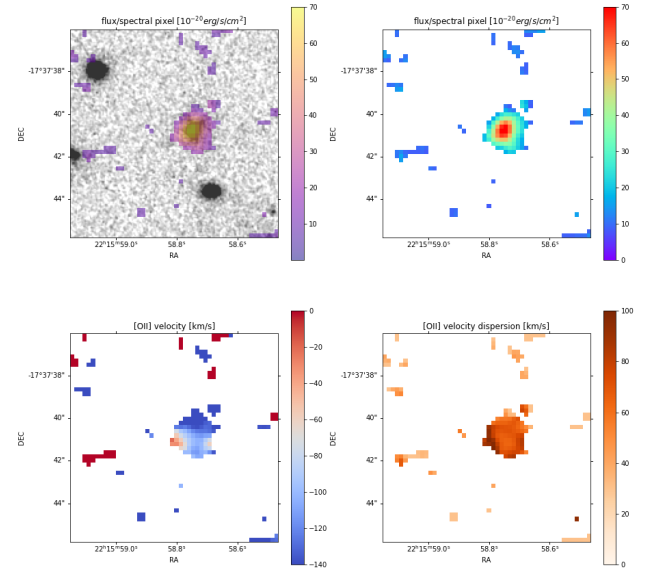


Fig. A.7: Clockwise starting at the upper left panel: HST F160W image around the galaxy 32152 hosting a type-2 AGN with overplotted [OII] EL map; spatially resolved [OII] EL map; spatially resolved [OII] velocity dispersion map; spatially resolved [OII] velocity map. The white background corresponds to spaxels with  $\text{SNR}_{[\text{OII}]} < 4$ . From ALMA, galaxy 32152 has a derived molecular gas mass of  $6.6^{+0.8}_{-0.9} \times 10^{10} M_{\odot}$  (Hayashi et al. 2018).

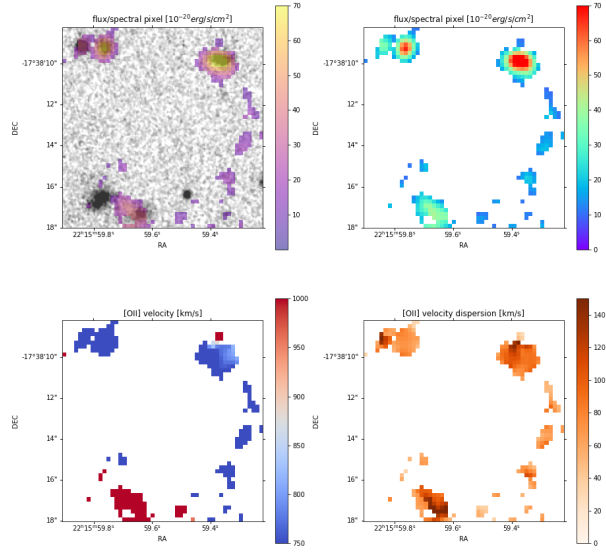


Fig. A.6: Clockwise starting at the upper left panel: HST F160W image including the galaxy 823 in the north-west upper part of the image, object 13 in the south part and another galaxy at slightly lower redshift in the north-east upper part of the image, with overplotted [OII] EL map; spatially resolved [OII] EL map; spatially resolved [OII] velocity dispersion map; spatially resolved [OII] velocity map. The white background corresponds to spaxels with  $\text{SNR}_{[\text{OII}]} < 4$ .

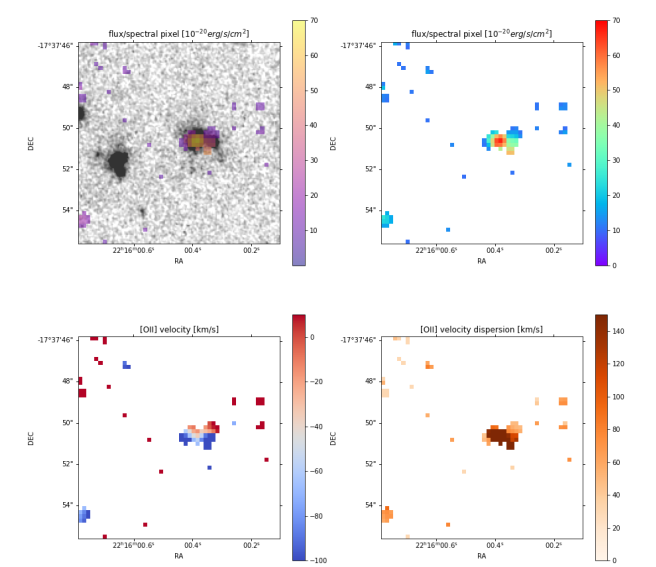


Fig. A.8: Clockwise starting at the upper left panel: HST F160W image around the galaxy 31746 hosting a type-2 AGN with overplotted [OII] EL map; spatially resolved [OII] EL map; spatially resolved [OII] velocity dispersion map; spatially resolved [OII] velocity map. The white background corresponds to spaxels with  $\text{SNR}_{[\text{OII}]} < 3$ . From ALMA, galaxy 31746 has a derived molecular gas mass of  $(3.2 \pm 0.6) \times 10^{10} M_{\odot}$  (Hayashi et al. 2018).